NJC

PAPER

View Article Online
View Journal | View Issue

Cite this: *New J. Chem.*, 2017, **41**, 7938

Cesium-doped graphene grown *in situ* with ultra-small TiO_2 nanoparticles for high-performance lithium-ion batteries†

Xiaoyu Lu, [ab] Xiaofeng Xie, [a] Jianqiang Luo[a] and Jing Sun *[a]

For applications of lithium-ion batteries (LIBs), to improve the electronic conductivity and the electrochemical kinetics of the electrode material, a novel composite of ultra-small TiO_2 nanoparticles grown *in situ* on cesium-doped reduced graphene oxide was prepared. The ultra-small TiO_2 nanoparticles (~7 nm), which were obtained by refluxing in anhydrous ethanol, were evenly distributed on the graphene surface, endowing high reactivity with Li^+. In particular, doping of graphene with Cs was proposed and was performed in the electrode material of LIBs by a facile method. The electron-doping effect of graphene was proved to increase the electronic conductivity of the composite. Benefiting from these properties, a Cs-doped rGO/TiO_2 (CsGT) electrode displayed good cyclability and particularly outstanding rate capability. The CsGT electrode exhibited a capacity of 163 mA h g^{-1} at 0.4C after 100 cycles, as well as a capacity of 109 mA h g^{-1} with a retention of 55.4% when the current density was increased to 20C, which was much better than the performance of control samples. At a current density of 40C, the CsGT electrode exhibited a highly reversible capacity of 70 mA h g^{-1} after 1000 cycles. The superiority of doping with Cs in comparison with calcination under a reducing atmosphere is carefully discussed *via* detailed characterization and electrochemical impedance spectroscopy (EIS) analysis.

Received 14th April 2017,
Accepted 24th June 2017

DOI: 10.1039/c7nj01251a

rsc.li/njc

1. Introduction

Owing to their high energy density, light weight and long cycle life, rechargeable lithium-ion batteries have gained increasing attention as the most promising power sources for portable devices and electric/hybrid vehicles.[1] Requirements for batteries with higher safety, higher rate capability and higher power density are still urgent, in particular in applications of electrical/hybrid vehicles.[2] TiO_2 has been regarded as a promising anode material for LIBs owing to its high reversible capacity, as well as low cost, non-toxicity and natural abundance.[3,4] With its relatively high lithium insertion/extraction voltage (~1.6 V *vs.* Li/Li^+), TiO_2 as the anode material could effectively avoid the formation of solid electrolyte interface (SEI) layers and the dendritic growth of Li, which cause capacity loss and risk problems. In addition, its low volume expansion (<4%) upon lithiation leads to high structural stability and a long cycle life.[5–7] However, the intrinsic drawbacks of its low electronic conductivity (~10^{-12} S cm^{-1}) and low diffusion coefficient in the solid phase (10^{-11}–10^{-13} cm^2 s^{-1}), which result in limited capacity and rate capability, have restricted its practical application in LIBs.[8] To overcome the sluggish diffusion of lithium ions, several strategies have been proposed, which include:[9,10] (i) reducing the ion diffusion length by fabricating nanostructured TiO_2 (particles, wires, tubes, *etc.*) and (ii) endowing TiO_2 with an amorphous shell, which facilitates the fast transport of lithium ions into the bulk TiO_2. The electronic conductivity can be increased by:[11–13] (i) introducing a conductive carbonaceous material such as graphene, CNTs and carbon coatings and (ii) doping with oxygen vacancies or heteroatoms (B,[14] C,[15] N,[16] *etc.*).

In comparison with CNTs and carbon coatings, graphene performs better as an electronically conductive additive owing to its continuous network for fast electron transport,[17] large surface to volume ratio, thermal/chemical stability and mechanical strength.[18] With respect to the agglomeration and dissolution of TiO_2 nanomaterials during charge–discharge cycles, graphene also possesses great advantages for dispersing and confining nano-TiO_2 owing to its unique 2D structure.[19] In a typical method of hybridization, graphene oxide and nano-TiO_2 were prepared separately, surface-modified, dispersed and subsequently mixed together,[6,20,21] which caused unavoidable agglomeration of TiO_2 and restacking of graphene sheets. Hence, an *in situ* strategy is

[a] *The State Key Lab of High Performance Ceramics and Superfine Microstructure, Shanghai Institute of Ceramics, Chinese Academy of Sciences, 1295 Ding Xi Road, Shanghai 200050, P. R. China. E-mail: jingsun@mail.sic.ac.cn; Fax: +86 21 52413122; Tel: +86 21 52414301*

[b] *University of Chinese Academy of Sciences, 19 Yuquan Road, Beijing 100049, P. R. China*

† Electronic supplementary information (ESI) available. See DOI: 10.1039/c7nj01251a

preferred for fabricating TiO_2/rGO composites.[17,22–24] Nevertheless, TiO_2 particle sizes are not small enough and the dispersion of nano-TiO_2 has not yet been satisfactory.[24]

Reduced graphene oxide is widely used owing to its ease of mass production and low production costs. However, oxygen-containing groups on the surfaces and edges produced by oxidation and few-layer stacking caused by inadequate exfoliation lead to low electronic conductivity and a relatively small specific surface area, respectively.[25] One way to increase its conductivity is to reduce graphene oxide by various means (thermal, hydrothermal, light emission, chemical reduction, *etc.*).[26] However, the increase is not satisfactory owing to the accompanying destruction of hexagonal carbon networks during reduction. Another way is to dope graphene with heteroatoms (N, B, S, *etc.*), which either fill defects in rGO or replace oxygen sites, although the additional doping process makes this inconvenient for applications in the TiO_2/rGO system.[27–29] It is known that typical rGO/GO, which has a high value of the work function (F_w), can only be regarded as a hole transport substrate in the optoelectronics research field,[30] which is also unfavorable for electron transport in LIBs. Doping with alkali metals has been investigated as a strategy for engineering the work function of graphene to improve its optoelectronic performance, but has yet to be applied in research on LIBs.[31,32] Among the alkali metals, Cs displays the highest electron-donating ability to reduce the value of F_w.[33] Moreover, Cs-doped GO/rGO can be readily obtained by mixing cesium carbonate with GO under mild conditions and easily isolated after the reduction of GO,[31] which makes it easy to incorporate into the preparation of TiO_2/rGO. On the basis of the above analysis, a combination of Cs-doped rGO and TiO_2 nanoparticles (NPs) grown *in situ* would improve the electrochemical performance of LIBs.

In this work, a well-designed Cs-doped rGO/TiO_2 composite was prepared. Firstly, Cs-doped GO was obtained by dispersing cesium carbonate in a GO solution. Subsequently, ultra-small TiO_2 nanoparticles ($\sim$7 nm) were grown *in situ* on Cs-doped rGO. As an electrode material for lithium-ion batteries, doping with Cs effectively increased the electronic conductivity of rGO, and the TiO_2 nanoparticles accelerated the diffusion of Li^+ ions by shortening the diffusion path, which were demonstrated by EIS analysis. The spaces between well-distributed TiO_2 nanoparticles also helped to buffer volume changes during discharge–charge cycles. Benefiting from these advantages, a CsGT electrode exhibited outstanding rate capability (109 mA h g^{-1} at 20C) and cyclability at a high current density (70 mA h g^{-1} at 40C after 1000 cycles), which were much superior to those of a sample prepared without doping with Cs. Further EIS analysis and SEM observations of the CsGT electrode during cycling testing confirmed its structural stability, which brings about good long-term cycling performance.

2. Experimental

2.1 Materials preparation

Preparation of CsGO. Graphene oxide (GO) was prepared using a modified Hummers' method[34,35] and dispersed in anhydrous ethanol. All the ethanol used in this experiment was pre-treated with a molecular sieve. Typically, 50 mg GO was first dispersed in 180 mL ethanol, and 12.5 mg Cs_2CO_3 (weight ratio of GO/Cs_2CO_3: 4 : 1) was first dissolved in 10 mL ethanol and then added to the GO solution dropwise. The mixture was stirred for 30 min at room temperature. For comparison, CsGO samples with different weight ratios (16 : 1, 8 : 1, 2 : 1, 1 : 1, and 1 : 2) were prepared.

Preparation of Cs-doped rGO/TiO_2 (CsGT). Firstly, 2.5 g tetrabutyl titanate (TBOT) was dissolved in 10 mL anhydrous ethanol and added to the above CsGO solution dropwise under intensive stirring for 10 min. A transparent brown solution was observed, which indicated that TBOT had not been hydrolyzed. Subsequently, 2 mL deionized water was dissolved in 10 mL ethanol and added to the mixture, which was placed in an oil bath at 100 °C and kept for 6 h. During this process, the solution gradually turned grey. The collected powder was washed with ethanol and distilled water three times each by centrifugation before undergoing a hydrothermal process at 180 °C for 6 h. The final Cs-doped rGO/TiO_2 product was obtained after washing with distilled water and was dried in a vacuum oven at 80 °C.

Preparation of rGO/TiO_2 (GT). As a control, GT was prepared *via* the same process as CsGT but without the addition of Cs_2CO_3.

Preparation of calcined rGO/TiO_2 (c-GT). c-GT was obtained by the calcination of GT at 450 °C for 1 h under an Ar/H_2 atmosphere (5% H_2, 95% Ar).

Preparation of calcined Cs-doped rGO/TiO_2 (c-CsGT). c-CsGT was obtained by the calcination of CsGT at 450 °C for 1 h under an Ar/H_2 atmosphere (5% H_2, 95% Ar).

Preparation of TiO_2. TiO_2 was prepared *via* the same process as GT but without the addition of GO.

2.2 Materials characterization

Thermogravimetric analysis was carried out using a NETZSCH STA 449C analyzer in the temperature range of 40–800 °C at a heating rate of 10 °C min^{-1} in air. The morphology of the samples was characterized with a field emission scanning microscope (Magellan 400, FEI) system and a transmission electron microscope (JEM-2100F at 200 kV). X-ray diffraction (XRD) was carried out with a D/max 2550V X-ray diffractometer with Cu Kα radiation at λ = 1.5406 Å. Raman spectra were recorded using a DXR Raman microscope (Thermo Scientific Corporation, USA) with an excitation wavelength of 532 nm. Fourier transform infrared (FT-IR) spectra were recorded with a Thermo Scientific Nicolet iN10 microscope. X-ray photoelectron spectroscopy (XPS) analysis was conducted using a twin-anode gun and Mg Kα radiation (1253.6 eV) (Microlab 310F scanning Auger microprobe, VG Scientific Ltd).

2.3 Electrochemical measurements

Cyclic voltammetry (CV) testing was conducted on a CHI660 electrochemical workstation in the voltage range of 3.0–1.0 V at a scan rate of 0.1 mV s^{-1}. Nyquist plots were recorded using the same workstation, and all half-cells were discharged to 1.0 V.

The active materials were mixed with acetylene black and a polyvinylidene fluoride (PVDF) binder in a weight ratio of 70 : 20 : 10 to form a uniform slurry. After the slurry was coated onto a copper foil, the electrode was dried in a vacuum oven at 80 °C for 20 h. The amount of active material in each cell was around 0.4–0.5 mg. The electrolyte used was 1 M $LiPF_6$ in a 50 : 50 (w/w) mixture of ethylene carbonate (EC) and dimethyl carbonate (DMC).

Half cells with lithium flake as the counter electrode were assembled into CR2016-type coin cells in an argon-filled glove box with concentrations of moisture and oxygen of less than 0.1 ppm. The discharge process corresponded to the lithiation reaction of the electrode material. The galvanostatic discharge/charge process was tested using a Land program-controlled battery testing system (CT2001A) over the voltage range of 1.0–3.0 V *versus* Li/Li^+.

3. Results and discussion

3.1. Characterization of cesium-doped GO

The route for the preparation of Cs-doped graphene/TiO_2 is illustrated in Scheme 1. GO and rGO sheets have abundant oxygen-containing groups (hydroxyl, carbonyl, epoxy and so on) on their surface,[36] which make them typical p-type doped graphene with low electronic conductivity. On the one hand, a large number of defects in graphene makes it difficult to establish a conducting network. On the other hand, oxygen-containing groups withdraw electrons from rGO and lead to slow electron transport, which is unfavorable for applications in LIBs. The use of cesium as an electron donor has been demonstrated, and it has been widely employed for doping graphene.[30,32] In contrast to doping with B/N, whereby hetero-atoms replace O atoms in GO/rGO, doping of graphene with Cs is a kind of chemical doping, in which electron-donating or electron-withdrawing groups are adsorbed on the surface of graphene.[37] Here, Cs carbonate was easily dissolved in an ethanolic solution, and the resulting Cs^+ ions were attracted to and adsorbed on negatively charged GO (Fig. S1, ESI†). As shown in Fig. 1a and b, owing to the introduction of the oppositely charged cation Cs^+ CsGO contains more wrinkles than pristine GO. When the weight ratio of GO/Cs_2CO_3 was decreased to less than 2 : 1 (w/w), the phenomenon of flocculation became severe in the CsGO suspension. We speculate that excess Cs^+ overcame the electrostatic repulsion and caused severe stacking and folding of GO sheets, which greatly reduced the specific surface area of GO and made it unsuitable for supporting TiO_2 as a 2D conducting network. EDS maps of CsGO are shown in Fig. 1c–f. After ultrasonication for several minutes, Cs and O elements were distributed homogeneously throughout the basal plane of CsGO sheets, which is attributed to the strong interaction between Cs^+ and oxygen-containing groups on GO.[31] According to elemental analysis (Fig. S2, ESI†), the Cs content in CsGO was determined to be about 19 wt% (Table S1, ESI†), which is very close to the feed ratio in the ethanolic solution (calculated to be around 17 wt%). Because almost all the Cs^+ ions were detected on the surface of GO, this method of doping with Cs proved effective in such mild conditions. Fig. 2 shows the FT-IR transmittance spectra of GO and CsGO. Typical absorption peaks of GO are located at ~1734 cm^{-1} (carbonyl and carboxyl C=O vibrations), ~1642 cm^{-1} (C=C skeletal vibrations), 1240 cm^{-1} (epoxy C–O stretching vibrations) and 1010 cm^{-1} (C–O stretching vibrations).[38,39] In the spectrum of CsGO, the intensities of peaks assigned to C–O and epoxy C–O stretching vibrations decreased and the C=O vibration peak even disappeared. This change demonstrates the intense interaction between Cs ions and oxygen-containing groups on GO.

To further determine the effect of doping with Cs and to optimize the amount of the Cs dopant, we recorded Raman spectra of CsGO with varying feed ratios of Cs_2CO_3 to GO. Theoretical and experimental research has demonstrated that pristine graphene exhibits a typical G band located at around 1580 cm^{-1},[37] which is sensitive to chemical doping. In n-type doped graphene with adsorbed molecules with electron-donating groups, the G band is downshifted, whereas it is upshifted in p-type doped graphene.[37] Fig. 3 shows the statistical results that represent the G band positions of CsGO and

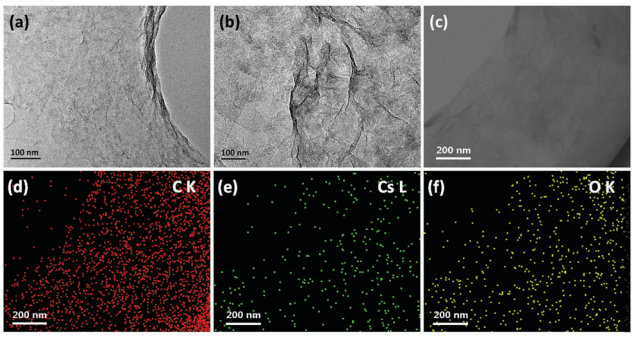

Fig. 1 TEM images of (a) pristine GO and (b) CsGO; (c) TEM image of CsGO and the corresponding elemental mapping images of (d) C, (e) Cs and (f) O.

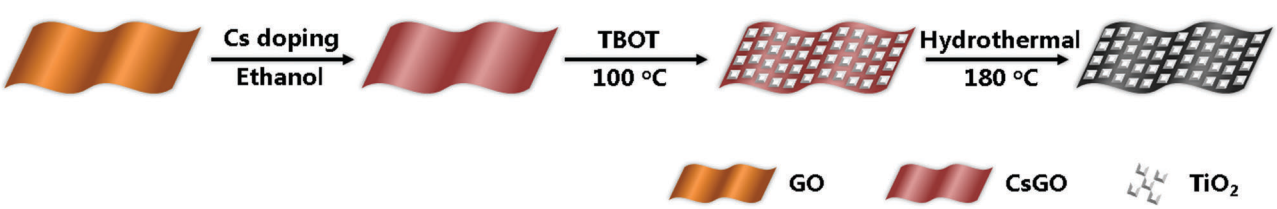

Scheme 1 Schematic of the synthesis procedure of CsGT.

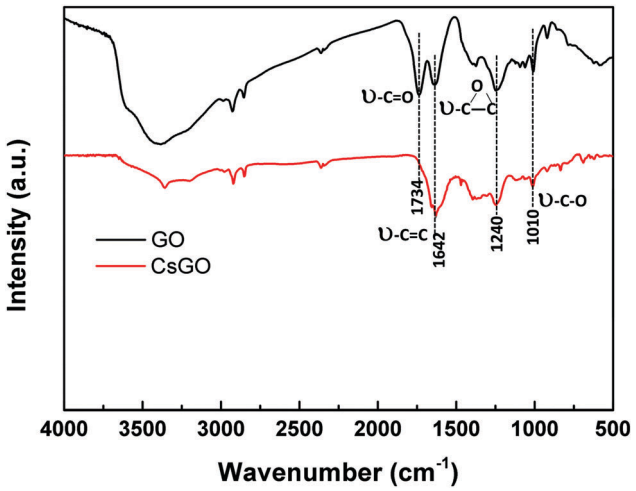

Fig. 2 FT-IR spectra of GO and the CsGO composite.

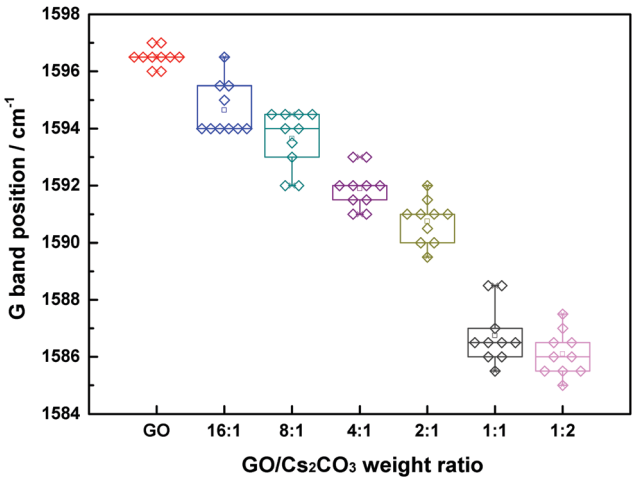

Fig. 3 Statistical results for G band positions in Raman tests with respect to variations in the weight ratio of GO/Cs_2CO_3.

GO, for which Raman spectra were recorded for 10 random points on each sample. The G band of the original GO is positioned at around 1596.5 cm^{-1}, and the adsorption of Cs^+ ions on the surface obviously changed the electronic state of GO. With a decrease in the weight ratio of GO/Cs_2CO_3 from 16 : 1 to 8 : 1, 4 : 1, 2 : 1, 1 : 1 and 1 : 2, the average position of the G band was gradually downshifted from 1595 to 1594, 1592, 1591, 1587 and 1586 cm^{-1}. This trend reveals that the degree of p-doping was gradually reduced with an increase in the amount of Cs_2CO_3.[37] As we have discussed, when the ratio of GO/Cs_2CO_3 is less than 2 : 1, severe agglomeration and stacking would destroy the structure of pristine GO. In addition, it is inferred that CsGO (1 : 1) is almost fully doped with Cs, because the position of the G band changed little when the Cs amount was doubled from a ratio of 1 : 1 to 1 : 2. Moreover, in the TiO_2/rGO composite rGO usually occupies only 5–10 wt% of the whole composite, and Cs, which has no lithium storage ability, should not be present in an excessive weight ratio in the electrode material. For these reasons, the preparation of CsGO with a weight ratio of GO/Cs_2CO_3 of 4 : 1 is rational and effective for this work.

3.2. Characterization of CsGT and the control samples

During the refluxing process, pristine TiO_2 NPs grew and were homogeneously distributed on the CsGO surface owing to the ethanolic system in which TBOT was hydrolyzed slowly. After hydrothermal treatment, CsGO was reduced to Cs-doped rGO (CsrGO). The decomposition of Cs salts led to the formation of cesium oxide on rGO, which behaved as an electron-transporting layer.[31] The ultra-small TiO_2 particles in CsGT grown *in situ* with an average diameter of about 7 nm were evenly dispersed on CsrGO (Fig. 4a), which favors the fast diffusion of Li in TiO_2.[40] The particle size and dispersion of TiO_2 remained unchanged after the calcination process (Fig. 4b). TEM images (Fig. 4c–f) reveal more morphological details of CsGT and c-CsGT. The composites both exhibit a sheet-like structure in which Cs-doped rGO is fully decorated with TiO_2 NPs on both sides. The TiO_2 NPs display high electrochemical reactivity with the highly conductive CsrGO layer that lies between them. Closer observation of the TiO_2 NPs reveals that their sizes changed little after calcination

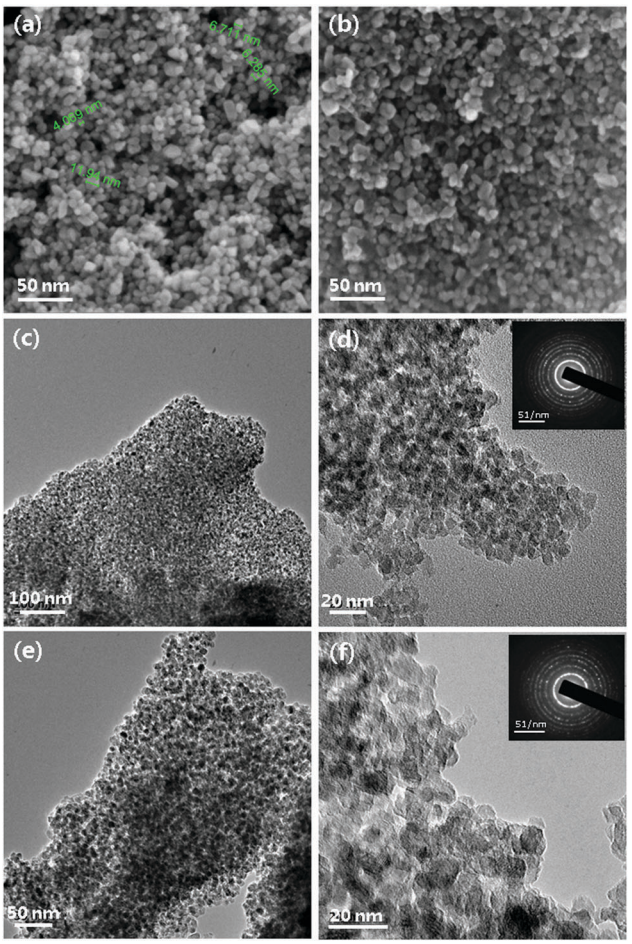

Fig. 4 SEM images of (a) CsGT and (b) c-CsGT; (c and d) TEM images of CsGT, with the corresponding SAED pattern in the inset of (d); (e and f) TEM images of c-CsGT, with the corresponding SAED pattern in the inset of (f).

under the reducing atmosphere. Some relatively large TiO_2 NPs in CsGT display a typical truncated octahedral anatase TiO_2 morphology with sharp edges (Fig. S3, ESI†). However, a thin surface layer of TiO_2 NPs in c-CsGT became amorphous as a result of oxygen vacancies introduced by reduction by H_2 during the calcination process (Fig. S4, ESI†), as expressed in the equation $TiO_2 + H_2 \rightarrow TiO_{2-x} + xH_2O$.[41] According to previous studies, the formation of an amorphous TiO_2 shell could establish a built-in electrical field that accelerates the diffusion of Li^+ ions into and out of the TiO_2 NPs,[10] resulting in enhanced lithium storage performance.

The XRD patterns of GT, CsGT, c-GT and c-CsGT are shown in Fig. 5a. The majority of peaks are well indexed to anatase TiO_2 (JCPDS no. 21-1272), but a weak peak of the brookite phase (JCPDS no. 29-1360) is also found at 30.5° ((121) facet). According to the half-widths of the main (101) facet peaks and the Scherrer equation, the average sizes of the TiO_2 particles were calculated to be 7.4 nm, 6.7 nm, 8.0 nm and 7.1 nm for GT, CsGT, c-GT and c-CsGT, respectively. In spite of partial surface reduction, the TiO_2 crystal particles became slightly larger after the calcination process. The Raman spectra of GT, CsGT, c-GT and c-CsGT indicate the coexistence of anatase TiO_2 and rGO (Fig. 5b and c). The spectrum of blank TiO_2 (Fig. 5b) displays four characteristic Raman vibration peaks of the anatase phase at 147.7 (E_g), 402.1 (B_{1g}), 518.8 (A_{1g} and B_{1g}) and 640.4 cm^{-1} (E_g).[42] For the graphene-containing composites, the peaks at 402.1, 518.8 and 640.4 cm^{-1} were downshifted to around 398.4, 513.8 and 634.0 cm^{-1}, respectively. The peaks around 398.4 and 634.0 cm^{-1} represent symmetric O–Ti–O bond stretching vibrations towards and away from Ti centers. The reduction in the vibration energy suggests a lengthening of Ti–O bonds because of the formation of Ti–O–C linkages between TiO_2 and graphene. These composites exhibit typical D and G bands. The D bands for the four samples are all located at around 1344 cm^{-1}, whereas the G bands exhibited a downshift of 6 cm^{-1} from 1601 to 1595 cm^{-1} after doping with Cs, which was caused by the electron-donating effect of Cs and also proves that the effect of doping with Cs was maintained after the hydrothermal and calcination processes.[31] Thermogravimetric analysis (TGA) was conducted to determine the graphene content in GT and c-GT. As shown in Fig. 5d, the weight loss below 200 °C was due to the evaporation of water. After being heated to 800 °C, GT and c-GT were completely converted to TiO_2, with overall weight losses of 9.1 wt% and 6.2 wt%, respectively. Thus, the graphene contents in GT and c-GT were calculated to be 9.6 wt% and 6.6 wt%, respectively. The decrease in the graphene ratio was caused by the further reduction of rGO by treatment at 450 °C in Ar/H_2, which also increased the conductivity of rGO. Assuming that the additional Cs had no influence on the other components and did not change during the hydrothermal and calcination treatments, the Cs content in CsGT and c-CsGT is around 3 wt%. Fig. 5e shows the wide-scan XPS spectrum of CsGT, which confirms the presence of C 1s, O 1s and Ti 2p. The core-level C 1s spectrum of CsGT consists of three main components, which are assigned to C–C/C═C (285.0 eV), C–O (286.8 eV) and C═O (289.1 eV) (Fig. S5, ESI†). CsGO was largely reduced by the hydrothermal process, as implied by the low amount of C–O/C═O bonds. The peaks with binding energies of 459.0 eV and 464.8 eV are attributed to Ti $2p_{3/2}$ and Ti $2p_{1/2}$, respectively, which implies that the principal Ti species in CsGT is Ti^{4+} (Fig. 5f).

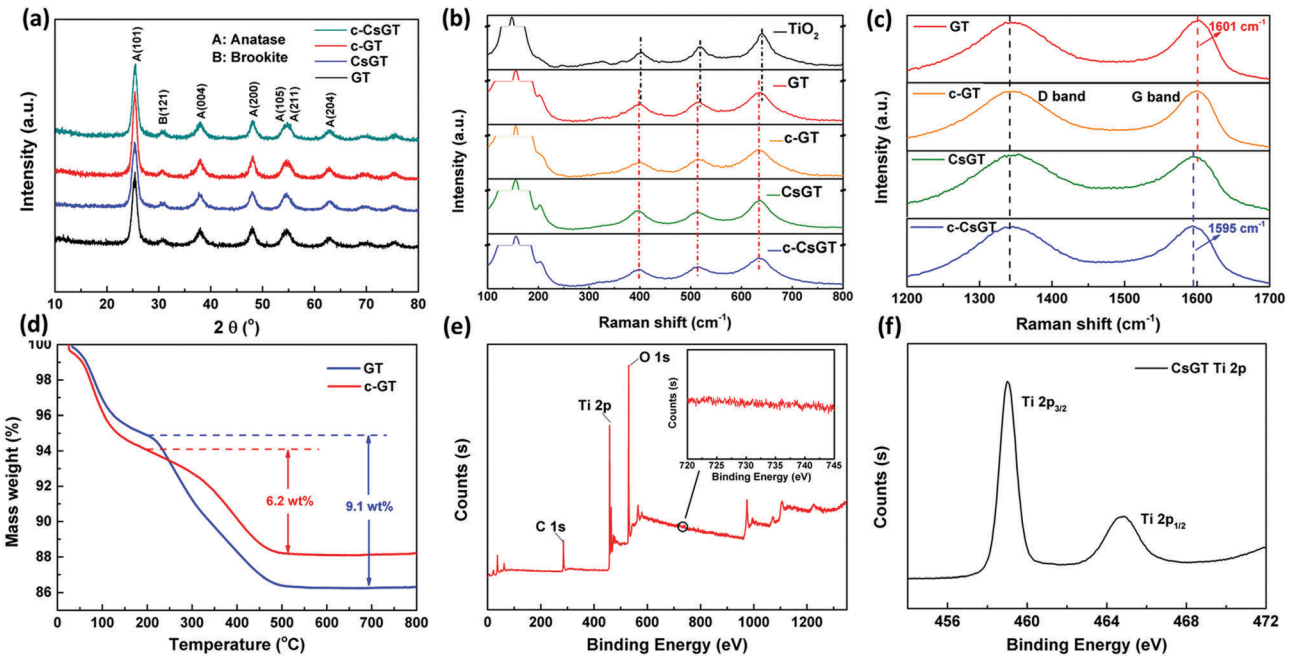

Fig. 5 Materials characterization: (a) XRD patterns of GT, c-GT, CsGT and c-CsGT; Raman spectra revealing (b) typical peaks of TiO_2, GT, c-GT, CsGT and c-CsGT and (c) D bands and G bands of graphene for GT, c-GT, CsGT and c-CsGT; (d) TG curves of GT and c-GT; (e) XPS survey spectrum and (inset) Cs 3d core-level XPS spectrum of CsGT; (f) Ti 2p core-level XPS spectrum of CsGT.

It is noteworthy that a typical signal of the Cs 3d core-level spectrum of CsGT was not found. We believe that there are two probable reasons for this: firstly, Cs element is located on the rGO surface and is fully covered with TiO_2 nanoparticles, which makes it difficult to detect by XPS. Secondly, the amount of Cs in CsGT (about 3 wt%) is too low to be detected. After further calcination, c-CsGT exhibited similar XPS peaks to those of CsGT, except that a characteristic Cs 3d core-level peak was found for c-CsGT (Fig. S6, ESI†). In other words, doping with Cs successfully changed the electronic properties with little influence on the composite morphology of graphene and TiO_2 NPs grown *in situ*. The calcination process changed not only the ratio of graphene in the composite but also the surface morphology of TiO_2.

3.3. Electrochemical performance of CsGT and the control samples

The influences of doping with Cs and surface reduction on the performance of rGO/TiO_2 samples were investigated by electrochemical tests. As anode materials for LIBs, all the electrode materials were assembled and tested in a half-cell system. To demonstrate the cyclability of CsGT, we performed a cyclic voltammetry test at a scan rate of 0.1 mV s^{-1} in the voltage range of 1.0–3.0 V. As shown in Fig. 6a, CsGT exhibited a main reduction peak at 1.7 V in the first cycle, which corresponds to the reduction of TiO_2 to Li_xTiO_2. Besides, the small reduction peak at around 1.5 V is characteristic of the further intercalation of Li beyond the tetragonal/orthorhombic phase boundary in TiO_2 particles with a diameter of less than 10 nm.[43] The intensities of both peaks were reduced slightly in the second cycle. Because the cut-off voltage was set at 1.0 V, no typical peaks due to the storage of Li by graphene were revealed in the CV curves. On the other hand, oxidation peaks at ~2.0 V, which are attributed to the oxidation of Li_xTiO_2 to TiO_2, were found in the first and subsequent anodic processes, with high reversibility. From the second sweep onward, the CV curves overlap one another, which indicates the high reversibility of the CsGT electrode during lithiation–delithiation reactions.

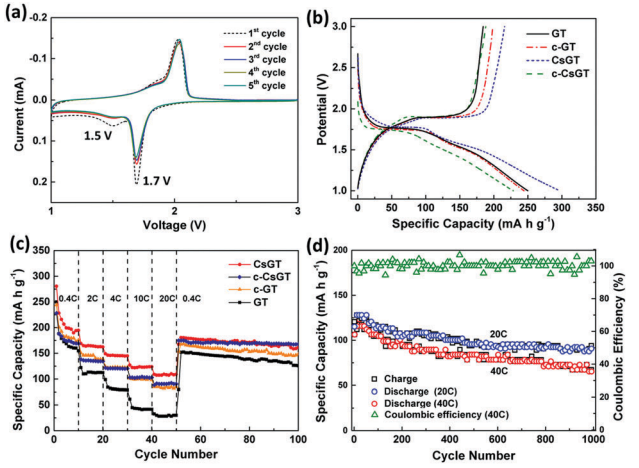

Fig. 6 (a) Cyclic voltammograms for the first 5 cycles of the CsGT electrode at a scan rate of 0.1 mV s^{-1}; (b) first discharge–charge voltage profiles of the GT, c-GT, CsGT and c-CsGT electrodes at a current density of 0.4C; (c) rate capabilities of the GT, c-GT, CsGT and c-CsGT electrodes at different current densities; (d) long-term cycling performance of the CsGT electrode at current density of 20C and 40C.

The long-term cycling performance and rate capability of the CsGT and control samples were determined by galvanostatic discharge–charge measurements at various current densities from 0.4C to 40C (1C equals 168 mA g^{-1}). According to the voltage profiles (Fig. 6b), the capacity of the electrodes comprised two parts: the intercalation of Li^+ into crystalline TiO_2 and interfacial lithium storage due to nano-sized TiO_2.[44] At a current density of 0.4C, the CsGT, c-CsGT, c-GT and GT electrodes exhibited initial discharge capacities of 292.3, 228.5, 244.3 and 249.9 mA h g^{-1}, respectively. The coulombic efficiencies of the first discharge–charge cycle for each sample were 74%, 82%, 81% and 74%, respectively. After 100 cycles, the reversible capacities were 163 (CsGT), 168 (c-CsGT), 147 (c-GT) and 130 (GT) mA h g^{-1}. In comparison with the c-CsGT, c-GT and GT electrodes, the CsGT electrode exhibited the best performance at high current densities owing to its increased electronic conductivity. When the current densities increased from 0.4C to 2C, 4C, 10C and 20C, the CsGT electrode exhibited a capacity retention of 84.6%, 74.8%, 63.6% and 55.4%, respectively (Fig. 6c). As a comparison, the c-CsGT, c-GT and GT electrodes only displayed a capacity retention of 53.2%, 47.2% and 17.6%, respectively, at 20C. The increased rate capability of CsGT shows the effectiveness of doping with Cs, which indicates that electronic conductivity may be the primary factor in the TiO_2/rGO system that restricts electronic charge exchange at high current density. The high rate capability of CsGT (109 mA h g^{-1} at 20C) is superior to those of reported TiO_2/graphene hybrid electrode materials, such as 105 mA h g^{-1} at 2.0 A g^{-1} (3D macroporous graphene/TiO_2 nanoparticles),[17] 90 mA h g^{-1} at 10C (graphene-wrapped hollow TiO_2 particles),[20] 112.2 mA h g^{-1} at 1.0 A g^{-1} (TiO_2 nanoparticles grown *in situ* on graphene),[24] 95 mA h g^{-1} at 1.2 A g^{-1} (atomic layer deposited amorphous TiO_2 on graphene sheets),[45] 80 mA h g^{-1} at 20C (minky dot fabric-shaped TiO_2 microsphere wrapped by graphene)[46] and 107 mA h g^{-1} at 20C (surfactant-assisted self-assembled anatase TiO_2/graphene).[23] However, it is comparable to or slightly lower than values such as 113.5 mA h g^{-1} at 30C (anatase TiO_2 submicrosphere wrapped by few-layer graphene),[6] 126 mA h g^{-1} at 18C (N-doped TiO_2 nanotube/N-doped graphene composite),[28] 103 mA h g^{-1} at 50C (surface-amorphized TiO_2@graphene composite)[8] and 115 mA h g^{-1} at 5 A g^{-1} (dandelion-shaped TiO_2/multi-layer graphene composite).[47] In a long-term battery test at current density of as high as 20C and 40C, the CsGT electrode displayed high reversible capacities of 89 and 70 mA h g^{-1} after 1000 cycles (Fig. 6d), and the capacity retention was 77% and 69%, respectively. The coulombic efficiency was maintained at nearly 100%. On the one hand, the nano-sized TiO_2 reduced the diffusion length of Li^+. On the other hand, the Cs-doped graphene, with its increased electronic conductivity, enabled faster electron transport. These two aspects ensured fast electron–Li^+ reactions in the electrode material, which improved the lithium storage performance, in particular, the outstanding rate capability.

As shown in Fig. 7, the discharge–charge voltage profiles of the different electrode samples further explained the effects of

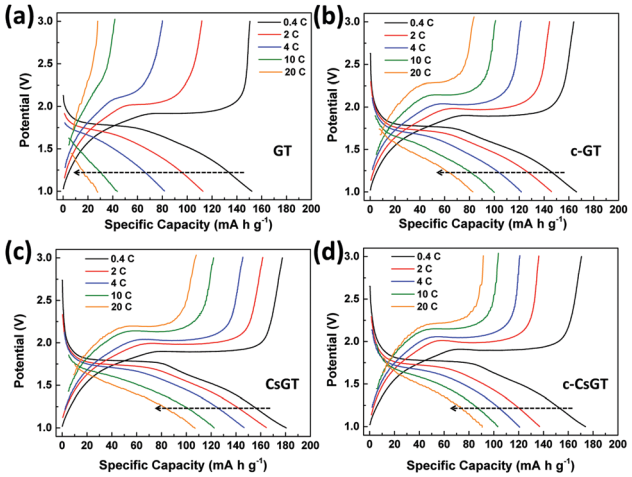

Fig. 7 Discharge–charge voltage profiles of (a) GT, (b) c-GT, (c) CsGT and (d) c-CsGT at different current densities (0.4C, 2C, 4C, 10C and 20C).

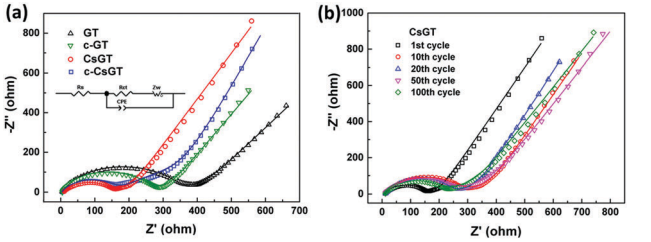

Fig. 8 Nyquist plots for the (a) GT, c-GT, CsGT and c-CsGT electrodes after the first discharge to 1.0 V and (b) the CsGT electrode after various numbers of cycles at a current density of 2C. The corresponding equivalent circuit model is shown in the inset of (a).

doping with Cs. For the GT electrode, the capacity declined drastically with an increase in the operating current, and the charging voltage plateaus disappeared above a rate of 4C. In comparison with GT, CsGT exhibited lower charging voltage plateaus and increased capacities at various current densities, which was attributed to the increased electronic conductivity of the composite. By comparing the charging voltage plateaus for different samples (Table S2, ESI†), it was found that the voltage hysteresis phenomenon for CsGT was the weakest among the four samples. In this work, c-GT exhibited higher capacity than GT because of the further reduction of rGO, which increased the electrical conductivity, and the amorphous TiO_2 shell, which accelerated the diffusion of Li^+ in TiO_2. However, the performance of c-CsGT was inferior to that of CsGT, which we will carefully discuss in the next section. The morphologies of the CsGT electrode after discharge–charge cycles are shown in Fig. S7 (ESI†). After 100 discharge–charge cycles, tiny TiO_2 nanoparticles remained well dispersed on CsrGO, which helped the electrode material to maintain its structural integrity and stability. Benefiting from enhanced electrochemical properties and structural stability, the CsGT electrode exhibited excellent rate capability and cycling performance.

3.4. Electrochemical impedance analysis and discussion

To confirm the excellent properties of the CsGT electrode, we performed electrochemical impedance spectroscopy (EIS) for comparison. Nyquist plots for all the samples are shown in Fig. 8a for the frequency range from 100 kHz to 0.01 Hz. The simulated results for resistance are listed in Tables S3 and S4 (ESI†). In the high- and intermediate-frequency regions, the semicircles for CsGT and c-CsGT are smaller than those for GT and c-GT, which indicates decreases in the electrolyte/electrode interfacial resistance and charge transfer resistance (R_{ct}). Although c-CsGT exhibited a similar R_{ct} value to CsGT, the low-frequency region for c-CsGT implies slower diffusion of Li^+ than that in CsGT. During the first 10 discharge–charge cycles, the R_{ct} value of CsGT increased owing to the irreversible insertion and extraction of Li^+, which is consistent with the capacity fade in the first few cycles. Afterwards, CsGT exhibited relatively steady values of R_{ct} and the Li^+ diffusion resistance, according to Fig. 8b. These results suggest that the structure and properties of CsGT were largely retained during battery cycling.

As discussed above, calcination treatment (450 °C in Ar/H_2 for 1 h) of GT, which increased the conductivity of rGO and created an amorphous surface of TiO_2 NPs, improved the electrochemical performance of c-GT in comparison with that of GT. In contrast, the performance of c-CsGT at high current densities was worse than that of CsGT. We believe that this deterioration was caused by the doping of TiO_2 with Cs. As shown in the Nyquist plots in Fig. S8 and the Bode phase plots in Fig. S9 (ESI†), the c-CsGT electrode displayed an additional specific resistance around 1–20 Hz, which usually corresponds to the diffusion of Li^+. This suggests an additional electrochemical reaction in the half-cell. As was reported, Cs can dope TiO_2 at crystal boundaries and defect sites.[48,49] The calcination process and the formation of an amorphous TiO_2 surface with a large amount of oxygen vacancies promoted this reaction.[48] As revealed in the XPS spectra of c-CsGT (Fig. S6, ESI†), the Cs core-level spectrum shows the presence of Cs, which was probably caused by the transport of some Cs from the inner rGO surface to the outer TiO_2 surface. On the one hand, Cs on the TiO_2 surface would cause sluggish diffusion of Li^+ into the crystal. On the other hand, the loss of Cs doping of rGO reduces the electronic conductivity of the whole electrode.

4. Conclusions

In summary, we have developed a novel and facile Cs doping method for designing a CsrGO/TiO_2 composite as a high-performance anode material for LIBs. Highly crystalline TiO_2 NPs with a size of ~7 nm were homogeneously anchored on Cs-doped rGO. Doping of rGO with Cs was accomplished *via* intense interactions between Cs^+ and oxygen-containing groups under moderate conditions. In applications of lithium-ion battery electrodes, Cs-doped rGO with increased electronic conductivity and nano-sized TiO_2 can help to accelerate the transport of electrons and Li^+ and to buffer changes in the volume of TiO_2 in the electrode. As a consequence, the as-prepared CsGT

electrode exhibited superior rate capability and long-term cycling performance in comparison to the GT, c-GT and c-CsGT electrodes. The high structural stability of CsGT was revealed by a high-rate (40C) battery test over 1000 cycles, with capacity attenuation of only 31%. Our work highlights the advantages of doping rGO with Cs when utilized in the electrodes of LIBs, which could be applied to other graphene-based materials and opens up new prospects for the modification of graphene in applications in the field of energy storage.

Acknowledgements

This work is financially supported by the National Key Research and Development Program of China (Grant No. 2016YFA0203000) and the National Natural Science Foundation of China (Grant No. 51402340).

References

1 J. B. Goodenough and Y. Kim, *Chem. Mater.*, 2010, **22**, 587–603.
2 K. V. Sreelakshmi, S. Sasi, A. Balakrishnan, N. Sivakumar, A. S. Nair, S. V. Nair and K. R. V. Subramanian, *Energy Technol.*, 2014, **2**, 257–262.
3 Q. Zhang, E. Uchaker, S. L. Candelaria and G. Cao, *Chem. Soc. Rev.*, 2013, **42**, 3127–3171.
4 P. G. Bruce, B. Scrosati and J. M. Tarascon, *Angew. Chem.*, 2008, **47**, 2930–2946.
5 Y. S. Hu, L. Kienle, Y. G. Guo and J. Maier, *Adv. Mater.*, 2006, **18**, 1421–1426.
6 J. Peng, G. Wang, Y.-T. Zuo, G. Li, F. Yu, B. Dai and X.-H. Guo, *RSC Adv.*, 2016, **6**, 20741–20749.
7 Y. Liu and Y. Yang, *J. Nanomater.*, 2016, **2016**, 1–15.
8 T. Zhou, Y. Zheng, H. Gao, S. Min, S. Li, H. K. Liu and Z. Guo, *Adv. Sci.*, 2015, **2**, 1500027.
9 M. Søndergaard, Y. Shen, A. Mamakhel, M. Marinaro, M. Wohlfahrt-Mehrens, K. Wonsyld, S. Dahl and B. B. Iversen, *Chem. Mater.*, 2015, **27**, 119–126.
10 T. Xia, W. Zhang, J. Murowchick, G. Liu and X. Chen, *Nano Lett.*, 2013, **13**, 5289–5296.
11 A. L. Mohana Reddy, S. R. Gowda, M. M. Shaijumon and P. M. Ajayan, *Adv. Mater.*, 2012, **24**, 5045–5064.
12 I. Moriguchi, R. Hidaka, H. Yamada, T. Kudo, H. Murakami and N. Nakashima, *Adv. Mater.*, 2006, **18**, 69–73.
13 R. Leary and A. Westwood, *Carbon*, 2011, **49**, 741–772.
14 S. In, A. Orlov, R. Berg, F. Garcia, S. Pedrosa-Jimenez, M. S. Tikhov, D. S. Wright and R. M. Lambert, *J. Am. Chem. Soc.*, 2007, **129**, 13790–13791.
15 J. H. Park, S. Kim and A. J. Bard, *Nano Lett.*, 2006, **6**, 24–28.
16 R. Asahi, T. Morikawa, T. Ohwaki, K. Aoki and Y. Taga, *Science*, 2001, **293**, 269–271.
17 F. Li, J. Jiang, X. Wang, F. Liu, J. Wang, Y. Chen, S. Han and H. Lin, *RSC Adv.*, 2016, **6**, 3335–3340.
18 C. Xu, B. Xu, Y. Gu, Z. Xiong, J. Sun and X. S. Zhao, *Energy Environ. Sci.*, 2013, **6**, 1388.
19 M. Yu, J. Ma, H. Song, A. Wang, F. Tian, Y. Wang, H. Qiu and R. Wang, *Energy Environ. Sci.*, 2016, **9**, 1495–1503.
20 J. S. Chen, Z. Wang, X. C. Dong, P. Chen and X. W. Lou, *Nanoscale*, 2011, **3**, 2158–2161.
21 R. Meng, H. Hou, X. Liu, J. Duan and S. Liu, *J. Porous Mater.*, 2015, **23**, 569–575.
22 X. Xin, X. Zhou, J. Wu, X. Yao and Z. Liu, *ACS Nano*, 2012, **6**, 11035–11043.
23 D. Wang, D. Choi, J. Li, Z. Yang, Z. Nie, R. Kou, D. Hu, C. Wang, L. V. Saraf, J. Zhang, I. A. Aksay and J. Liu, *ACS Nano*, 2009, **3**, 907–914.
24 H. Liu, K. Cao, X. Xu, L. Jiao, Y. Wang and H. Yuan, *ACS Appl. Mater. Interfaces*, 2015, **7**, 11239–11245.
25 R. Raccichini, A. Varzi, S. Passerini and B. Scrosati, *Nat. Mater.*, 2015, **14**, 271–279.
26 L. U. Xiaoyu, X. H. Jin and J. Sun, *Sci. China: Technol. Sci.*, 2015, **58**, 1829–1840.
27 Z. S. Wu, W. Ren, L. Xu, F. Li and H. M. Cheng, *ACS Nano*, 2011, **5**, 5463–5471.
28 Y. Li, Z. Wang and X.-J. Lv, *J. Mater. Chem. A*, 2014, **2**, 15473.
29 D. Cai, D. Li, S. Wang, X. Zhu, W. Yang, S. Zhang and H. Wang, *J. Alloys Compd.*, 2013, **561**, 54–58.
30 J. Liu, Y. Xue, Y. Gao, D. Yu, M. Durstock and L. Dai, *Adv. Mater.*, 2012, **24**, 2228–2233.
31 J. H. Huang, J. H. Fang, C. C. Liu and C. W. Chu, *ACS Nano*, 2011, **5**, 6262–6271.
32 J. D. Lin, C. Han, F. Wang, R. Wang, D. Xiang, S. Qin, X. A. Zhang, L. Wang, H. Zhang, A. T. Wee and W. Chen, *ACS Nano*, 2014, **8**, 5323–5329.
33 K. C. Kwon, K. S. Choi, B. J. Kim, J.-L. Lee and S. Y. Kim, *J. Phys. Chem. C*, 2012, **116**, 26586–26591.
34 W. S. Hummers and R. E. Offeman, *J. Am. Chem. Soc.*, 1958, **80**, 1339.
35 C. Xu, J. Sun and L. Gao, *J. Mater. Chem.*, 2011, **22**, 975–979.
36 M. Du, C. Xu, J. Sun and L. Gao, *J. Mater. Chem. A*, 2013, **1**, 7154–7158.
37 H. Liu, Y. Liu and D. Zhu, *J. Mater. Chem.*, 2011, **21**, 3335–3345.
38 M. Zong, Y. Huang, Y. Zhao, X. Sun, C. Qu, D. Luo and J. Zheng, *RSC Adv.*, 2013, **3**, 23638–23648.
39 R. Wang, Y. Wang, C. Xu, J. Sun and L. Gao, *RSC Adv.*, 2013, **3**, 1194–1200.
40 X. Yang, Y. Yang, H. Hou, Y. Zhang, L. Fang, J. Chen and X. Ji, *J. Phys. Chem. C*, 2015, **119**, 3923–3930.
41 J.-Y. Shin, J. H. Joo, D. Samuelis and J. Maier, *Chem. Mater.*, 2012, **24**, 543–551.
42 J. Qiu, C. Lai, Y. Wang, S. Li and S. Zhang, *Chem. Eng. J.*, 2014, **256**, 247–254.
43 J.-Y. Shin, D. Samuelis and J. Maier, *Adv. Funct. Mater.*, 2011, **21**, 3464–3472.
44 M. Wagemaker and F. M. Mulder, *Acc. Chem. Res.*, 2013, **46**, 1206.
45 M. Li, X. Li, W. Li, X. Meng, Y. Yu and X. Sun, *Electrochem. Commun.*, 2015, **57**, 43–47.

46 C. Zha, D. He, J. Zou, L. Shen, X. Zhang, Y. Wang, H. H. Kung and N. Bao, *J. Mater. Chem. A*, 2014, **2**, 16931–16938.
47 W. Song, J. Chen, X. Ji, X. Zhang, F. Xie and D. J. Riley, *J. Mater. Chem. A*, 2016, **4**, 8762–8768.
48 M. Zamora, T. López, M. Asomoza, R. Meléndrez and R. Gómez, *Catal. Today*, 2006, **116**, 234–238.
49 S. Kwon, K.-G. Lim, M. Shim, H. C. Moon, J. Park, G. Jeon, J. Shin, K. Cho, T.-W. Lee and J. K. Kim, *J. Mater. Chem. A*, 2013, **1**, 11802.

